CHINESE OPTICS LETTERS

Vol. 22, No. 1 | January 2024

Experimental demonstration of a flexible-grid 1 × (2 × 3) mode- and wavelength-selective switch using silicon microring resonators and counter-tapered couplers

Dejun Kong (孔德军)[1], Hao Lu (鲁 昊)[1], Pengjun Wang (汪鹏君)[2*], Qiang Fu (符 强)[3], Shixun Dai (戴世勋)[1,4], Weiwei Chen (陈伟伟)[1**], Yuefeng Wang (王栎沣)[1], Bohao Zhang (张波豪)[1], Lingxiao Ma (马凌霄)[1], Jun Li (李 军)[1], Tingge Dai (戴庭舸)[5], and Jianyi Yang (杨建义)[5]

[1] Faculty of Electrical Engineering and Computer Science, Ningbo University, Ningbo 315211, China

[2] College of Electrical and Electronic Engineering, Wenzhou University, Wenzhou 325035, China

[3] College of Science and Technology, Ningbo University, Ningbo 315300, China

[4] Laboratory of Infrared Materials and Devices, The Research Institute of Advanced Technologies, Ningbo University, Ningbo 315211, China

[5] Department of Information Science and Electronics Engineering and Cyrus Tang Center for Sensor Materials and Applications, Zhejiang University, Hangzhou 310027, China

*Corresponding author: wangpengjun@wzu.edu.cn

**Corresponding author: chenweiwei@nbu.edu.cn

Received June 7, 2023 | Accepted August 15, 2023 | Posted Online January 2, 2024

A flexible-grid 1 × (2 × 3) mode- and wavelength-selective switch which comprises counter-tapered couplers and silicon microring resonators has been proposed, optimized, and demonstrated experimentally in this work. By carefully thermally tuning phase shifters and silicon microring resonators, mode and wavelength signals can be independently and flexibly conveyed to any one of the output ports, and different bandwidths can be generated as desired. The particle swarm optimization algorithm and finite difference time-domain method are employed to optimize structural parameters of the two-mode (de)multiplexer and crossing waveguide. The bandwidth-tunable wavelength-selective optical router composed of 12 microring resonators is studied by taking advantage of the transfer matrix method. Measurement results show that, for the fabricated module, cross talk less than −10.18 dB, an extinction ratio larger than 17.41 dB, an in-band ripple lower than 0.79 dB, and a 3-dB bandwidth changing from 0.38 to 1.05 nm are obtained, as the wavelength-channel spacing is 0.40 nm. The corresponding response time is measured to be 13.64 μs.

Keywords: integrated optics; optical waveguide; mode- and wavelength-selective switch.

DOI: 10.3788/COL202422.011301

1. Introduction

Because of the explosive growth of bandwidth (BW)-intensive applications, network traffic is boosting dramatically[1,2]. To handle the ever-increasing network traffic demands, novel technologies are desired to update optical networks to improve spectrum efficiency and transmission capacity. With the characteristic of fine-grained BW allocation, elastic optical networks (EONs) allow efficient spectrum utilization[3,4]. In addition, space division multiplexing (SDM) is a technology that exploits the core or mode as an independent data channel to further expand capacity[5,6]. Hence, combining EONs with SDM can offer a promising solution for tackling the capacity limitation[7,8].

In SDM-EONs, the flexible-grid mode- and wavelength-selective switch (MWSS) in which spatial and spectral resources can be allocated independently and flexibly is considered one of the crucial elements[9,10]. Due to its CMOS-compatible property, MWSSs in silicon photonics platforms have aroused increased research interest. To date, a number of MWSSs in different configurations have been presented. A 1 × 2 switch comprising mode (de)multiplexers and switching modules based on silicon microring resonators (MRRs) has been experimentally demonstrated[11]. This device can support four data channels, which contain two transverse-electric (TE) modes at two wavelengths. An MWSS possessing an add/drop function that is composed of silicon MRRs and Mach–Zehnder interferometers has been reported[12]. The proposed MWSS also can have four data channels, including two wavelength channels and two mode channels. Although the above MWSSs can have good performance, they do not possess BW-tunable properties. In order to attain

efficient spectrum utilization, flexible-grid MWSSs, which are suitable for SDM-EONs, are highly desired. In our previous work, a design of silicon flexible-grid MWSS based on Y-junctions and double-series coupled MRRs has been proposed and analyzed[13]. However, to the best of our knowledge, the experimental demonstration of a flexible-grid $1 \times (2 \times 3)$ MWSS has never before been discussed.

In this Letter, a flexible-grid $1 \times (2 \times 3)$ MWSS consisting of seven two-mode (de)multiplexers using counter-tapered couplers and two BW-tunable wavelength-selective optical routers (BTWSORs) utilizing reconfigurable add-drop silicon MRRs is designed, fabricated, and characterized in detail. To achieve a relatively compact size, a small insertion loss (IL), and a low cross talk (CT), the particle swarm optimization (PSO) algorithm and the finite difference time-domain (FDTD) method are used for optimizing structural parameters of the two-mode (de)multiplexer and crossing waveguide. The transfer matrix method is utilized to numerically study behaviors and properties of the BTWSOR. The optimized flexible-grid $1 \times (2 \times 3)$ MWSS is demonstrated experimentally on a silicon-on-insulator (SOI) platform. For the fabricated module, an extinction ratio (ER) > 17.41 dB, a CT < -10.18 dB, an in-band ripple (IBR) < 0.79 dB, and the 3-dB BW changing from 0.38 to 1.05 nm are measured as the wavelength-channel spacing $\Delta\lambda$ is 0.40 nm. The corresponding response time of 13.64 μs is obtained.

2. Principle and Design

Figure 1(a) shows the schematic diagram of the mentioned flexible-grid $1 \times (2 \times 3)$ MWSS, which is composed of a two-mode demultiplexer based on a counter-tapered coupler marked as TD_{I0}, six two-mode multiplexers based on counter-tapered couplers labeled as TD_{Oi} ($i = 1, 2, \ldots, 6$), and two BW-tunable wavelength-selective optical routers containing 24 reconfigurable add-drop silicon MRRs denoted by R_{Up} and R_{Dp} ($p = 1, 2, \ldots, 12$). Figures 1(b) and 1(c) show the detailed drawing and corresponding cross-sectional view of the two-mode

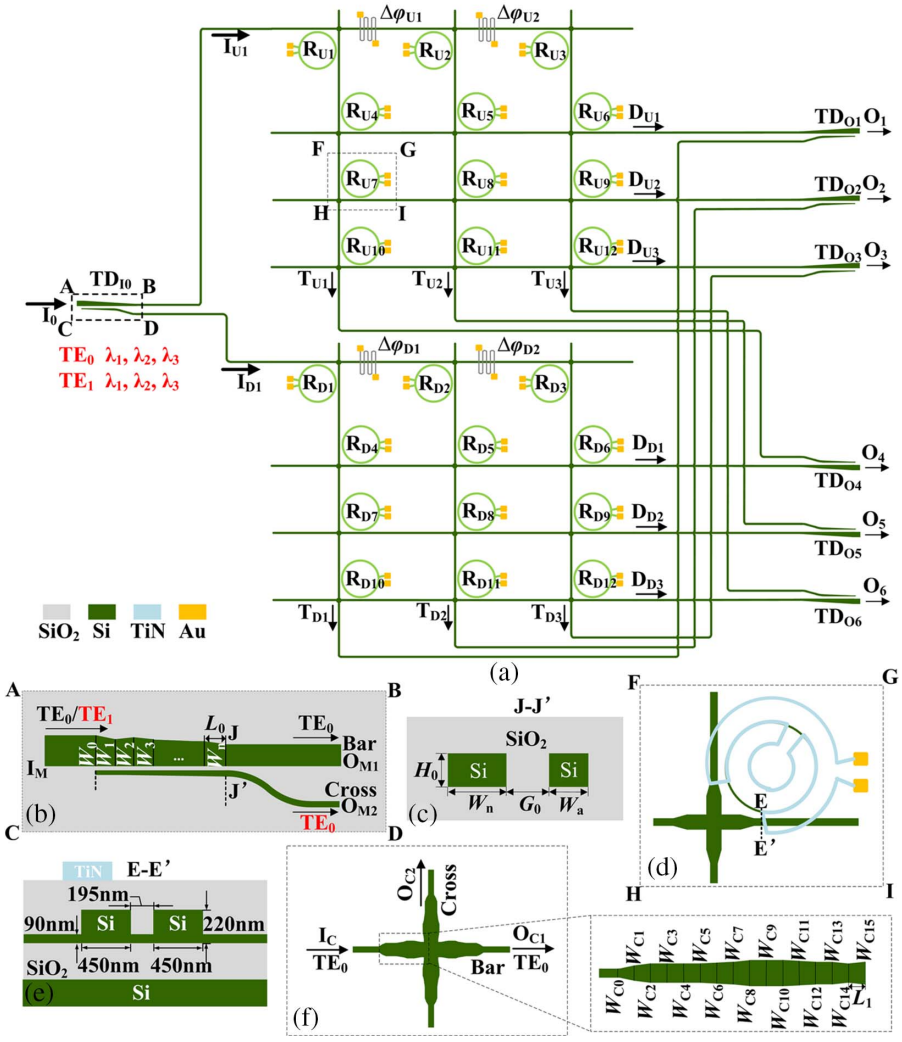

Fig. 1. (a) Schematic diagram of the flexible-grid $1 \times (2 \times 3)$ MWSS; (b) detailed drawing and (c) cross-sectional view of the proposed two-mode (de)multiplexer; (d) schematic diagram and (e) cross-sectional view of the mentioned silicon MRR; (f) structure of the proposed crossing waveguide.

Table 1. Typical States of the Presented Flexible-grid $1 \times (2 \times 3)$ MWSS in the Worst Situation.

States	Output Ports					
	01	02	03	04	05	06
1	TE_0-λ_2	TE_0-λ_3	TE_0-λ_1	TE_1-λ_2	TE_1-λ_3	TE_1-λ_1
2	TE_0-λ_3	TE_0-λ_2	TE_0-λ_1	TE_1-λ_3	TE_1-λ_2	TE_1-λ_1
3	TE_1-λ_3	TE_0-λ_2	TE_0-λ_1	TE_0-λ_3	TE_1-λ_2	TE_1-λ_1
4	TE_0-λ_2	TE_1-λ_3	TE_1-λ_1	TE_1-λ_2	TE_0-λ_3	TE_0-λ_1
5	TE_1-λ_3	TE_0-λ_2	TE_1-λ_1	TE_1-λ_2	TE_0-λ_3	TE_0-λ_1
6	TE_1-λ_2	TE_0-λ_3	TE_1-λ_1	TE_1-λ_3	TE_0-λ_2	TE_0-λ_1
7	TE_0-λ_1	TE_1-λ_2	TE_1-λ_3	TE_1-λ_1	TE_0-λ_2	TE_0-λ_3
8	TE_1-λ_1	TE_1-λ_2	TE_1-λ_3	TE_0-λ_1	TE_0-λ_2	TE_0-λ_3
9		TE_0-λ_1-λ_3		TE_1-λ_1-λ_3		
10		TE_0-λ_2, λ_3	TE_0-λ_1		TE_1-λ_2, λ_3	TE_1-λ_1
11		TE_0-λ_1, λ_3	TE_0-λ_2		TE_1-λ_1, λ_3	TE_1-λ_2
12		TE_0-λ_1, λ_2	TE_0-λ_3		TE_1-λ_1, λ_2	TE_1-λ_3
13		TE_0-λ_3	TE_0-λ_1, λ_2		TE_1-λ_3	TE_1-λ_1, λ_2
14		TE_0-λ_2	TE_0-λ_1, λ_3		TE_1-λ_2	TE_1-λ_1, λ_3
15		TE_0-λ_1	TE_0-λ_2, λ_3		TE_1-λ_1	TE_1-λ_2, λ_3
16			TE_0-λ_1-λ_3			TE_1-λ_1-λ_3

(de)multiplexer. The schematic diagram and cross-sectional view of the reconfigurable add-drop silicon MRR are illustrated in Figs. 1(d) and 1(e). Figure 1(f) depicts the structure of the adopted crossing waveguide. For R_{Up} and R_{Dp}, the corresponding resonance wavelengths are named λ_{Up} and λ_{Dp}. To adjust the path phase differences $\Delta\varphi_{U1}$, $\Delta\varphi_{U2}$, $\Delta\varphi_{D1}$, and $\Delta\varphi_{D2}$, phase shifters are designed in straight waveguides. In Fig. 1(a), the presented device supports 2×3 data channels, comprising two TE modes at three wavelengths. By employing the two-mode demultiplexer, all mode channels are converted into the fundamental mode. After then, for each mode channel, by carefully adjusting the resonance of silicon MRRs and path phase differences, the signal is wavelength-demultiplexed and then is routed flexibly with the BW-adjustable property. Finally, mode multiplexers are utilized to guarantee mode and wavelength signals can be conveyed to any one of the output ports, and different BWs are generated as required. Table 1 lists the typical states in the worst situation.

To investigate the behaviors and properties of the presented device, the two-mode (de)multiplexer is first designed. As seen in Fig. 1(b), if the effective refractive index of TE_1 mode in the bus waveguide is matched with that of TE_0 mode in the neighboring tapered waveguide, the conversion between the TE_1 mode in the bus waveguide and the TE_0 mode in the adjacent taper waveguide will be achieved. In this work, the PSO algorithm and FDTD method are adopted to optimize the structural parameters of the two-mode (de)multiplexer involved to realize compact size and good performance.

Table 2. Optimized Segments' Widths for the Bus Waveguide in the Coupling Region.

Symbol	Value/μm	Symbol	Value/μm	Symbol	Value/μm
W_0	0.85	W_1	0.85	W_2	0.74
W_3	0.75	W_4	0.78	W_5	0.71
W_6	0.62	W_7	0.62	W_8	0.58
W_9	0.59	W_{10}	0.45		

As seen in Fig. 1(b), the bus waveguide is separated into n ($n \geq 1$) equilong segments. The segments' length and width are marked as L_0 and W_m ($m = 0, 1, 2, \ldots, n$). In the simulation, the optimization figure of merit (FOM) is defined as $\mathrm{FOM}_1 = P_{\mathrm{Cross\_TE1\_TE0}}$ in the case of $1 \leq m \leq n-3$, while in the case of $n-2 \leq m \leq n$, the definition of the FOM is described as $\mathrm{FOM}_2 = \min(P_{\mathrm{Cross\_TE1\_TE0}}/P_{\mathrm{Bar\_TE1}}, P_{\mathrm{Bar\_TE0}}/P_{\mathrm{Cross\_TE0\_TE0}})$. Here, $P_{\mathrm{Cross\_TE1\_TE0}}$ is the optical power of the TE_0 mode obtained from the port O_{M2}, and $P_{\mathrm{Bar\_TE1(TE0)}}$ is the optical power of the TE_1 (TE_0) mode obtained from the port O_{M1}, as the TE_1 (TE_0) mode is input into the port I_M. The segment's width and the corresponding variation range are considered as the particle's position and velocity, which is renewed by employing the following equations[14,15]:

$$\mathrm{ve}_{l+1} = w_{\mathrm{T}} \times \mathrm{ve}_l + r_1 \times \gamma_1 \times (\mathrm{ib}_l - \mathrm{ps}_l) + r_2 \times \gamma_2 \times (\mathrm{gb}_l - \mathrm{ps}_l), \tag{1}$$

$$\mathrm{ps}_{l+1} = \mathrm{ps}_l + \mathrm{ve}_l, \tag{2}$$

where ve_l ($l = 1, 2, \ldots$) and ps_l represent the particle's velocity and position, w_{T} is the inertial weight, ib_l and gb_l are the individual and global best positions, the cognitive and social rates are denoted by r_1 and r_2, and γ_1 and γ_2 are the random numbers distributed uniformly between 0 and 1, respectively.

Table 2 summarizes the optimal widths of segments. In the optimization, the length L_0 is chosen to be 1 μm, the thickness H_0 is 220 nm, the width W_a is selected as $W_a = 300$ nm, the gap G_0 is 200 nm, r_1 and r_2 are set to be 2, and w_{T} is selected to be 1.

For the mentioned BTWSOR, each wavelength signal from the I_{U1} (I_{D1}) port could be transmitted to any of the ports T_{U1} (T_{D1}), T_{U2} (T_{D2}), T_{U3} (T_{D3}), D_{U1} (D_{D1}), D_{U2} (D_{D2}), and D_{U3} (D_{D3}). Furthermore, via R_{U1} (R_{D1}), R_{U2} (R_{D2}), and R_{U3} (R_{D3}) in the first row, the wavelength signals from the port I_{U1} (I_{D1}) are demultiplexed; then, via R_{U4} (R_{D4}), R_{U5} (R_{D5}), and R_{U6} (R_{D6}) in the second row, R_{U7} (R_{D7}), R_{U8} (R_{D8}), and R_{U9} (R_{D9}) in the third row, or R_{U10} (R_{D10}), R_{U11} (R_{D11}), and R_{U12} (R_{D12}) in the fourth row, the wavelength-demultiplexed signals from neighboring channels going through equal-length

optical paths are combined, and the corresponding transmission spectra with tunable BWs are implemented on demand at the ports D_{U1} (D_{D1}), D_{U2} (D_{D2}), and D_{U3} (D_{D3}). In order to study the mentioned BTWSOR, the transfer matrix method is utilized. The transfer functions of the optical router at the ports D_{U1} (D_{D1}), D_{U2} (D_{D2}), D_{U3} (D_{D3}), T_{U1} (T_{D1}), T_{U2} (T_{D2}), and T_{U3} (T_{D3}) are described below,

$$\begin{aligned} D_{U(D)1} = {} & \mathrm{Dr}_{U(D)1} \cdot \mathrm{Dr}_{U(D)4} \cdot \xi \cdot \mathrm{Th}_{U(D)5} \cdot \xi \cdot \mathrm{Th}_{U(D)6} + \mathrm{Th}_{U(D)1} \\ & \cdot \xi \cdot e^{-j\Delta\varphi_{U(D)1}} \cdot \mathrm{Dr}_{U(D)2} \cdot \mathrm{Dr}_{U(D)5} \cdot \xi \cdot \mathrm{Th}_{U(D)6} + \mathrm{Th}_{U(D)1} \\ & \cdot \xi \cdot e^{-j\Delta\varphi_{U(D)1}} \cdot \mathrm{Th}_{U(D)2} \cdot \xi \cdot e^{-j\Delta\varphi_{U(D)2}} \cdot \mathrm{Dr}_{U(D)3} \cdot \mathrm{Dr}_{U(D)6}, \end{aligned} \tag{3}$$

$$\begin{aligned} D_{U(D)2} = {} & \mathrm{Dr}_{U(D)1} \cdot \mathrm{Th}_{U(D)4} \cdot \xi \cdot \mathrm{Dr}_{U(D)7} \cdot \xi \cdot \mathrm{Th}_{U(D)8} \cdot \xi \cdot \mathrm{Th}_{U(D)9} \\ & + \mathrm{Th}_{U(D)1} \cdot \xi \cdot e^{-j\Delta\varphi_{U(D)1}} \cdot \mathrm{Dr}_{U(D)2} \cdot \mathrm{Th}_{U(D)5} \cdot \xi \cdot \mathrm{Dr}_{U(D)8} \\ & \cdot \xi \cdot \mathrm{Th}_{U(D)9} + \mathrm{Th}_{U(D)1} \cdot \xi \cdot e^{-j\Delta\varphi_{U(D)1}} \cdot \mathrm{Th}_{U(D)2} \\ & \cdot \xi \cdot e^{-j\Delta\varphi_{U(D)2}} \cdot \mathrm{Dr}_{U(D)3} \cdot \xi \cdot \mathrm{Th}_{U(D)6} \cdot \mathrm{Dr}_{U(D)9}, \end{aligned} \tag{4}$$

$$\begin{aligned} D_{U(D)3} = {} & \mathrm{Dr}_{U(D)1} \cdot \mathrm{Th}_{U(D)4} \cdot \xi \cdot \mathrm{Th}_{U(D)7} \cdot \xi \cdot \mathrm{Dr}_{U(D)10} \cdot \xi \cdot \mathrm{Th}_{U(D)11} \\ & \cdot \xi \cdot \mathrm{Th}_{U(D)12} + \mathrm{Th}_{U(D)1} \cdot \xi \cdot e^{-j\Delta\varphi_{U(D)1}} \cdot \mathrm{Dr}_{U(D)2} \\ & \cdot \xi \cdot \mathrm{Th}_{U(D)5} \cdot \xi \cdot \mathrm{Th}_{U(D)8} \cdot \mathrm{Dr}_{U(D)11} \cdot \xi \cdot \mathrm{Th}_{U(D)12} + \mathrm{Th}_{U(D)1} \\ & \cdot \xi \cdot e^{-j\Delta\varphi_{U(D)1}} \cdot \mathrm{Th}_{U(D)2} \cdot \xi \cdot e^{-j\Delta\varphi_{U(D)2}} \cdot \mathrm{Dr}_{U(D)3} \cdot \xi \cdot \mathrm{Th}_{U(D)6} \\ & \cdot \xi \cdot \mathrm{Th}_{U(D)9} \cdot \mathrm{Dr}_{U(D)12}, \end{aligned} \tag{5}$$

$$T_{U(D)1} = \mathrm{Dr}_{U(D)1} \cdot \xi \cdot \mathrm{Th}_{U(D)4} \cdot \xi \cdot \mathrm{Th}_{U(D)7} \cdot \xi \cdot \mathrm{Th}_{U(D)10}, \tag{6}$$

$$\begin{aligned} T_{U(D)2} = {} & \mathrm{Th}_{U(D)1} \cdot \xi \cdot e^{-j\Delta\varphi_{U(D)1}} \cdot \mathrm{Dr}_{U(D)2} \cdot \xi \cdot \mathrm{Th}_{U(D)5} \cdot \xi \\ & \cdot \mathrm{Th}_{U(D)8} \cdot \xi \cdot \mathrm{Th}_{U(D)11}, \end{aligned} \tag{7}$$

$$\begin{aligned} T_{U(D)3} = {} & \mathrm{Th}_{U(D)1} \cdot \xi \cdot e^{-j\Delta\varphi_{U(D)1}} \cdot \mathrm{Th}_{U(D)2} \cdot \xi \cdot e^{-j\Delta\varphi_{U(D)2}} \cdot \mathrm{Dr}_{U(D)3} \\ & \cdot \xi \cdot \mathrm{Th}_{U(D)6} \cdot \xi \cdot \mathrm{Th}_{U(D)9} \cdot \xi \cdot \mathrm{Th}_{U(D)12}, \end{aligned} \tag{8}$$

$$\mathrm{Th}_{U(D)i} = \frac{\sqrt{1-k^2}(1-\alpha e^{-j\theta_{U(D)i}})}{1-\alpha(1-k^2)e^{-j\theta_{U(D)i}}}, \tag{9}$$

$$\mathrm{Dr}_{U(D)i} = \frac{\alpha^{\frac{1}{4}} k^2 e^{-j\frac{\theta_{U(D)i}}{4}}}{1-\alpha(1-k^2)e^{-j\theta_{U(D)i}}}, \tag{10}$$

where $\mathrm{Dr}_{U(D)p}$ and $\mathrm{Th}_{U(D)p}$ represent the drop and through transmission of $R_{U(D)p}$, the scattering loss at each crossing is denoted by ξ, k is the field coupling coefficient of $R_{U(D)p}$, α is the corresponding field transmission coefficient, and $\theta_{U(D)p}$ is the round-trip phase shift of $R_{U(D)p}$.

To decrease the scattering loss ξ, the PSO algorithm and FDTD method are utilized to optimize structural parameters of the crossing waveguide involved. As seen in Fig. 1(f), the crossing waveguide involved consists of two identical multimode waveguides, which are orthogonal. For each multimode waveguide, the input and output tapers are mirror-symmetrical. The taper is separated into 15 equilong segments. The segments' length and width are denoted as L_1 and W_{Cs} ($s = 0, 1, 2, \ldots, 15$). Here, the definition of the FOM is written as $\mathrm{FOM}_3 = P_{\mathrm{CBar\_TE0}}$, where $P_{\mathrm{CBar\_TE0}}$ represents the optical power of the TE_0 mode obtained from the port O_{C1} with the TE_0 mode input into the port I_C. The segment's width and the corresponding variation range are regarded as the particle's position and velocity, which are renewed utilizing Eqs. (1) and (2). Table 3 lists the optimized segments' widths. In the optimization, the length L_1 is chosen to be 0.3 μm, and the slab thickness H_1 is 90 nm. Thus, ξ is calculated as $\xi = 0.08$ dB/crossing.

Table 3. Optimized Segments' Widths for the Taper in the Crossing Waveguide.

Symbol	Value/μm	Symbol	Value/μm	Symbol	Value/μm
W_{C0}	0.45	W_{C1}	0.70	W_{C2}	0.86
W_{C3}	0.88	W_{C4}	0.90	W_{C5}	0.90
W_{C6}	0.96	W_{C7}	1.04	W_{C8}	1.16
W_{C9}	1.16	W_{C10}	1.16	W_{C11}	1.10
W_{C12}	1.06	W_{C13}	1.06	W_{C14}	0.90
W_{C15}	1.00				

Figure 2 illustrates the working principle of forming the tunable BW. Take the spectrum with large BW at the port D_{U3} as an example. As shown in Figs. 1(a) and 2, optical signals with wavelengths of λ_{U1}, λ_{U2}, and λ_{U3} are separated when the light beam passes through the wavelength demultiplexer. Then, as R_{U1}, R_{U2}, R_{U3}, R_{U10}, R_{U11}, and R_{U12} are turned on, the separated signals, which pass equal-length optical paths, are coherently combined so that the spectrum with large BW can emerge from the port D_{U3}. In the simulation, the field transmission coefficient α is 0.9989 (a propagation loss of 1.52 dB/cm), the group refractive index is 3.8, and the radii of silicon MRRs are 10 μm, making the bend-related loss negligible[16,17]. The channel spacing in wavelength $\Delta\lambda$ is set as $\Delta\lambda = \lambda_{U1} - \lambda_{U2} = \lambda_{U2} - \lambda_{U3} = 0.4$ nm. To form flat-top spectra, the path phase differences $\Delta\varphi_{U1}$ and $\Delta\varphi_{U2}$ are optimized to be 0.5π. The gap G_1 is 195 nm, and thus the field coupling coefficient is 0.465.

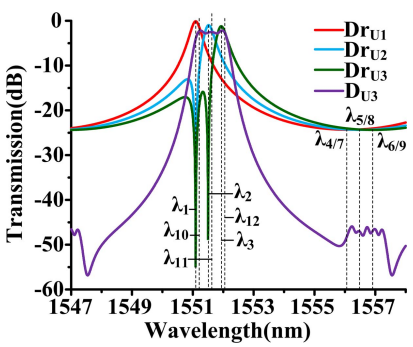

Fig. 2. Working principle of forming the tunable BW.

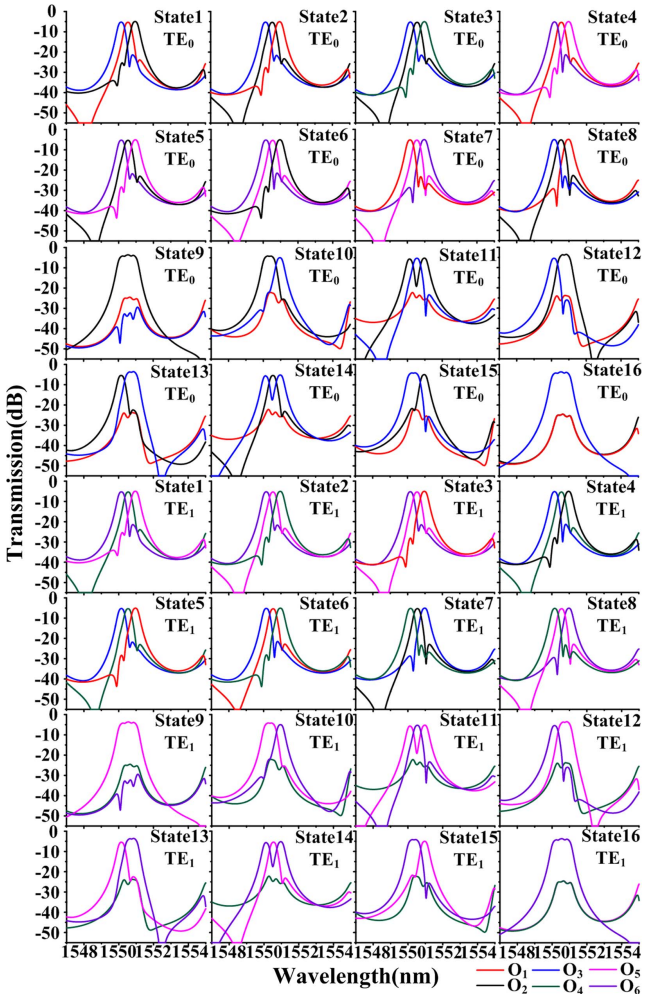

Fig. 3. Simulated transmission spectra of the designed silicon-based flexible-grid 1 × (2 × 3) MWSS in the typical states.

Figure 3 shows the transmission spectra of the designed flexible-grid 1 × (2 × 3) MWSS in the typical states, which is shown in Table 1. As described in Fig. 3, it is found that, the 3-dB BW ranges from 0.38 to 1.09 nm, the IL is smaller than 5.67 dB, and the IBR is lower than 0.68 dB, as $\Delta\lambda$ is set as 0.40 nm. For the input TE_0 mode, an ER $>$ 18.96 dB and a CT $<$ −10.98 dB are achieved; while for the input TE_1 mode, the ER is greater than 18.96 dB, and the corresponding CT is less than −10.83 dB.

The simulated maximum IL, worst CT, and minimum ER of the designed flexible-grid 1 × (2 × 3) MWSS or the designed flexible-grid 1 × (2 × 3) MWSS cascaded with a mode multiplexer and six mode demultiplexers as a function of the waveguide width variation ΔW are shown in Fig. 4. As the value of ΔW deviates from $\Delta W = 0$ nm, the IL changes significantly and grows larger, while the CT and ER change slightly and get worse. Note that in Fig. 4(a), in the case of the designed flexible-grid 1 × (2 × 3) MWSS, when ΔW ranges from −20 nm to 20 nm, the IL increases from 5.64 to 11.25 dB, the ER changes from 17.13 to 18.96 dB, and the CT varies from −9.98 to −10.83 dB. From Fig. 4(b), in the case of the designed flexible-grid 1 × (2 × 3) MWSS cascaded with a mode multiplexer and six mode demultiplexers, the corresponding IL increases from 6.22 to 13.38 dB, the ER changes from 17.11 to 18.96 dB, and the CT ranges from −9.97 to −10.79 dB when ΔW increases from −20 to 20 nm. From Figs. 4(a) and 4(b), it also can be found that, as the value of ΔW gradually stays away from 0, the IL of the cascaded mode (de)multiplexer would grow larger, while the ER and CT for the two cases above are basically unchanged.

3. Fabrication and Characterization

The designed flexible-grid 1 × (2 × 3) MWSS was fabricated on an 8-inch (20.3 cm) SOI wafer via commercial CMOS-compatible technologies at the Institute of Microelectronics, Singapore. Figure 5 shows the microscope image of the fabricated module comprising a flexible-grid 1 × (2 × 3) MWSS cascaded with a mode multiplexer and six mode demultiplexers.

A broadband light source and an optical spectrum analyzer are utilized for characterizing the fabricated devices first. A TE-type grating coupler is employed to couple the light beam into or out of the fabricated devices. By thermally tuning phase shifters and silicon MRRs, the corresponding transmission spectra can be recorded. By subtracting the transmission of the nearby straight waveguide, the measured optical power transmission of the fabricated module is normalized. Figure 6 shows the measured transmission spectra of the fabricated

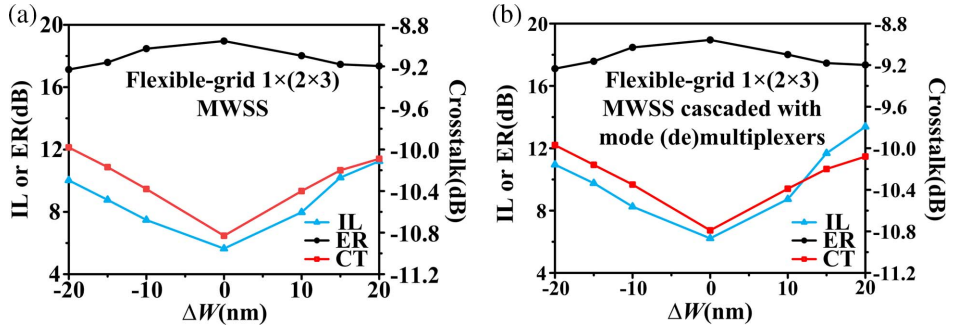

Fig. 4. Simulated maximum IL, worst CT, and minimum ER of (a) the designed flexible-grid 1 × (2 × 3) MWSS or (b) the designed flexible-grid 1 × (2 × 3) MWSS cascaded with a mode multiplexer and six mode demultiplexers changing with ΔW.

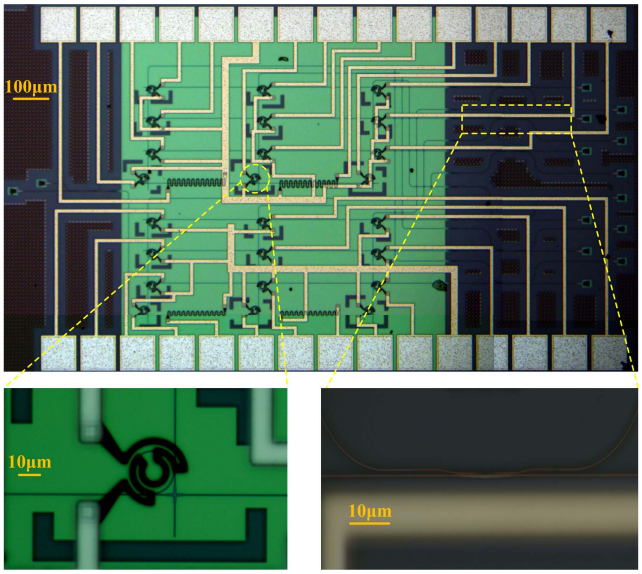

Fig. 5. Microscope image of the fabricated module.

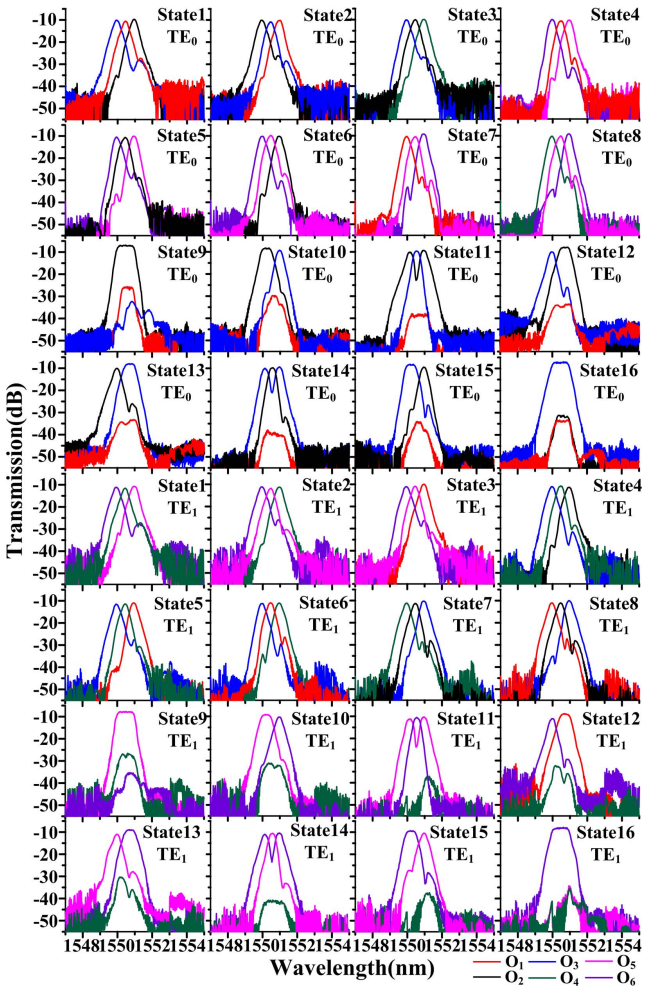

Fig. 6. Measured transmission spectra of the fabricated module.

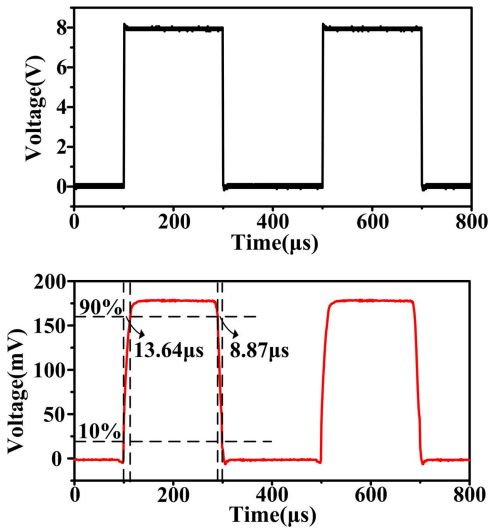

Fig. 7. Measured dynamic response of the fabricated device.

module. As described in Fig. 6, for the fabricated module, a CT < -10.18 dB, an ER > 17.41 dB, a maximum IL of 11.55 dB, a 3-dB BW ranging from 0.38 to 1.05 nm, and an IBR < 0.79 dB are measured. The maximum power consumption (PC) is 301.21 mW. As seen in Figs. 4(b) and 6, it is found that the actual width of the fabricated waveguide deviates from the optimal value owing to the process deviation. Under this situation, ΔW is extrapolated as $\Delta W = 15$ nm, and thus the maximum IL of the fabricated MWSS is about 10 dB. The measured dynamic response is characterized by employing the tunable laser, photodiode detector, oscilloscope, and signal generator. State 16 is taken as an example to explain the measurement. As described in Fig. 7, the dynamic response at the port O_3 would be recorded, when a 5-kHz square-wave signal in which the high-level and low-level voltages are 8 V and 0 V is loaded onto the heaters of R_{U1}, R_{U2}, R_{U3}, R_{U10}, R_{U11}, and R_{U12}. Note that in Fig. 7, the 10%–90% rise time of 13.64 μs and 90%–10% fall time of 8.87 μs can be measured. In future work, the IL can be reduced by using high-quality fabrication processes with a finer minimum feature size. Additionally, to further improve the CT and ER, double-series coupled MRRs could be used for enhancing the roll-off characteristic and decreasing the optical output power of unwanted wavelengths. The plasma dispersion effect can be adopted to raise the operation speed.

4. Conclusion

In conclusion, a flexible-grid $1 \times (2 \times 3)$ MWSS consisting of seven two-mode (de)multiplexers using counter-tapered couplers and two BTWSORs using silicon MRRs has been designed and experimentally demonstrated. By using the FDTD method and the PSO algorithm, we optimize the structural parameters of the two-mode (de)multiplexer and crossing waveguide to achieve relatively compact size, small IL, and low CT. The behaviors and properties of the BTWSOR are investigated by using the transfer matrix method. The optimized flexible-grid

$1 \times (2 \times 3)$ MWSS is fabricated on an SOI platform to verify its feasibility. As $\Delta\lambda$ is 0.40 nm, a CT of < -10.18 dB, an ER > 17.41 dB, an IBR < 0.79 dB, a 3-dB BW ranging from 0.38 to 1.05 nm, and a maximum PC of 301.21 mW are measured. The corresponding response time is 13.64 μs. With these characteristics, the mentioned flexible-grid $1 \times (2 \times 3)$ MWSS can be an attractive candidate for switching applications in SDM-EONs.

Acknowledgements

This work was supported by the National Natural Science Foundation of China (Nos. 62275134, 62234008, 61875098, and 61874078), the Zhejiang Provincial Natural Science Foundation (Nos. LY20F050003 and LY20F050001), the Natural Science Foundation of Ningbo (Nos. 2022J099 and 202003N4159), the Youth Science and Technology Innovation Leading Talent Project of Ningbo (No. 2023QL003), and the K. C. Wong Magna Fund at Ningbo University.

References

1. R. J. Zhu, S. H. Li, P. S. Wang, *et al.*, "Energy-efficient deep reinforced traffic grooming in elastic optical networks for cloud–fog computing," IEEE Internet Things J. **8**, 12410 (2021).
2. H. Yang, Y. S. Liang, J. Q. Yuan, *et al.*, "Distributed blockchain-based trusted multidomain collaboration for mobile edge computing in 5G and beyond," IEEE Trans. Industr. Inform. **16**, 7094 (2020).
3. B. W. Chen, Y. Lei, Y. F. Jiang, *et al.*, "Spectrum sharing-maximized approaches with shared-path protection in elastic optical data center networks," IEEE Internet Things J. **9**, 4721 (2021).
4. R. Koch, S. Kuhl, R. M. Morais, *et al.*, "Reinforcement learning for generalized parameter optimization in elastic optical networks," J. Lightwave Technol. **40**, 567 (2021).
5. G. Rademacher, B. J. Puttnam, R. S. Luis, *et al.*, "Peta-bit-per- second optical communications system using a standard cladding diameter 15-mode fiber," Nat. Commun. **12**, 4238 (2021).
6. K. Shibahara, T. Mizuno, and Y. Miyamoto, "Long-haul mode multiplexing transmission enhanced by interference cancellation techniques based on fast MIMO affine projection," J. Lightwave Technol. **38**, 4969 (2020).
7. P. M. Moura and N. L. S. Da Fonseca, "Multipath routing in elastic optical networks with space-division multiplexing," IEEE Commun. Mag. **59**, 64 (2021).
8. E. E. Moghaddam, H. Beyranvand, and J. A. Salehi, "Resource allocation in space division multiplexed elastic optical networks secured with quantum key distribution," IEEE J. Sel. Areas Commun. **39**, 2688 (2021).
9. M. Yang, Q. Wu, and Y. B. Zhang, "Joint assignment of spatial granularity, routing, modulation, and spectrum in SDM-EONs: minimizing the network CAPEX considering spectrum, WSS, and laser resources," J. Lightwave Technol. **36**, 4253 (2018).
10. M. C. Yang, Y. B. Zhang, and Q. Wu, "Routing, spectrum, and core assignment in SDM-EONS with MCF: node-arc ILP/MILP methods and an efficient XT-aware heuristic algorithm," J. Opt. Commun. Netw. **10**, 195 (2018).
11. B. Stern, X. L. Zhu, C. P. Chen, *et al.*, "On-chip mode-division multiplexing switch," Optica **2**, 530 (2015).
12. L. S. Han, B. P. P. Kuo, N. Alic, *et al.*, "Silicon photonic wavelength and mode selective switch for WDM-MDM networks," in *Optical Fiber Communications Conference and Exhibition (OFC)* (2019), p. 1.
13. W. W. Chen, H. Lu, P. J. Wang, *et al.*, "Silicon-based flexible-grid mode-and wavelength-selective switch utilizing microring resonators and Y-junctions," J. Lightwave Technol. **38**, 4000 (2020).
14. Y. Zhang, S. Y. Yang, A. E. J. Lim, *et al.*, "A compact and low loss Y-junction for submicron silicon waveguide," Opt. Express **21**, 1310 (2013).
15. W. W. Chen, B. H. Zhang, P. J. Wang, *et al.*, "Ultra-compact and low-loss silicon polarization beam splitter using a particle-swarm-optimized counter-tapered coupler," Opt. Express **28**, 30701 (2020).
16. D. N. Wu, Y. D. Wu, Y. Wang, *et al.*, "Reconfigurable optical add-drop multiplexer based on thermally tunable micro-ring resonators," Opt. Commun. **367**, 44 (2016).
17. T. Tsuchizawa, K. Yamada, H. Fukuda, *et al.*, "Microphotonics devices based on silicon microfabrication technology," IEEE J. Sel. Top. Quantum Electron. **11**, 232 (2005).